Supplementary Material

d-State Modulation in Cu_2SnS_4 Governs Electronic Transport Descriptors and VOC Sensing Selectivity: A DFT-BoltzTraP2 Study

Sathish Panneer Selvam [a*], Sungbo Cho [a,b,c*]

[a]*Department of Electronic Engineering, Gachon University, Seongnam-si, Gyeonggi-do 13120, Korea*

[b]*Department of Semiconductor Engineering, Gachon University, Seongnam-si, Gyeonggi-do 13120, Korea*

[c]*Gachon Advanced Institute for Health Science & Technology, Gachon University, Incheon 21999, Korea*

***Corresponding author:**

* Sathish Panneer Selvam: satp103@gachon.ac.kr

* Sungbo Cho: sbcho@gachon.ac.kr

Contents

Experimental Section

Contents

Results and Discussion

Experimental

S1 Computational details

First-principles DFT calculations were performed in CASTEP using ultrasoft pseudopotentials, the GGA-PBE exchange-correlation functional, and Grimme's DFT-D3 dispersion to capture noncovalent Van der Waals interactions critical for reliable structures and energetics ; on-site correlation for localized transition-metal d states was treated with the rotationally invariant DFT+U scheme with U_{eff} values of 4.0 eV (Mn-3d), 3.5 eV (Tc-4d), and 3.0 eV (Re-5d), guided by literature practice and calibrated for magnetic and electronic stability, consistent with established improvements of spin-state ordering, multiplet splittings, and geometries in transition-metal systems and the broader pseudohybrid perspective for accelerated, corrected electronic-structure screening[1,2] . A k-point grid convergence test was carried out by varying the k-point grid density to 6 × 6 × 8, 8 × 8 × 10, 10 × 10 × 12, and 12 × 12 × 14. The optimized k-point grid of 10 × 10 × 12 was considered the reference state, and the difference in total energy was calculated. Geometry optimizations for the primitive cell of Kesterite and Mn, Tc and Re-doped analogues used a 10 × 10 × 12 Monkhorst-Pack grid, a 450 eV plane-wave cutoff, and tight thresholds (force = 0.01 eV $Å^{-1}$; total energy change = 10^{-6} eV $atom^{-1}$), with spin polarization enabled for all doped systems and initial magnetic moments assigned according to expected oxidation states (Mn, Tc and Re=0.33), multiple magnetic orderings were tested to acknowledge the sensitivity of correlated d-electron materials. Electronic structures were obtained from band-structure calculations along a standard high-symmetry path for corresponding crystals (tetragonal and monoclinic) and from total/partial DOS computed on a denser 15 × 15 × 18 grid. To identify the minimum energy path (MEP) for the adsorption of VOCs on a Mn-integrated supercell of Cu2SnS4, we performed climbing image-nudged elastic band analysis with a threshold of 0.1 eV Å-1 set for 6 images, from the initial state (IS) to the final state (FS). We employed the Boltztrap2 tool to investigate the thermoelectric transport properties of the Zn, Mn, Tc, and Re-doped Cu_2SnS_4catalysts, in order to capture the SCF and NSCF calculations, Monkharst-pack k-points grid with the density of 20×20×24 under spin-polarized condition [3]. Phonon dispersion curves and the thermal properties of the crystals (temperature-

dependent Helmholtz free energy, heat capacity and entropy) were calculated using Phonopy, a Python-based software package which utilizes the supercell finite-displacement method [4].

S2 Monkhorst-Pack k-point grid convergence test

A Monkhorst-Pack k-point grid convergence test with respect to total-energy convergence was conducted for both doped and $ZnCu_2SnS_4$ systems. At a 10 × 10 × 12 grid, total energies were determined to converge within <1 meV for all compositions (Table S2). Partially filled d-states close to the Fermi level are the source of slightly greater oscillations seen for Tc- and Re-doped systems, which are consistent with their metallic nature [5]. Thus, to ensure consistent precision, a 10 × 10 × 12 grid was used for all extra computations.

S3 Doping analysis

To corroborate the efficient method of doping, we conducted substitutional and interstitial doping to identify the lowest formation energy exhibiting method of doping for feasibility. To evaluate the formation energy (E_f), the $ZnCu_2SnS_4$ system was considered as a pristine system, and its calculated total energy of the system is represented as $E_{pristine}$. In addition, the total energy of the metal-doped $ZnCu_2SnS_4$ has been denoted as E_{doped} , and the chemical potentials of Zn and M (Mn, Tc, and Re) were expressed as μ_{Zn} and μ_M, respectively [6].

$E_f = E_{doped} - E_{pristine} + \mu_{Zn} - \mu_M$ (for substitutional doping);

$E_f = E_{doped} - E_{pristine} - \mu_M$ (for interstitial doping);

Substitutional incorporation is energetically preferred over interstitial incorporation for all dopants considered. Substitutional formation energies are markedly lower (1.65-4.45 eV) compared to interstitial configurations (3.22-5.59 eV). This distinct energy separation signifies that dopant

atoms preferentially occupy lattice positions instead of interstitial spaces under equilibrium growth conditions. The persistently elevated E_f for interstitial defects (>3 eV) indicates that these configurations are thermodynamically unfavorable and unlikely to exist in significant concentrations [6].

A comparison analysis indicates a definite trend dependent on the dopant. Mn demonstrates the lowest formation energy in both substitutional (1.65 eV) and interstitial (3.22 eV) configurations, establishing it as the most thermodynamically stable dopant among the three Table S3). This behaviour aligns with the advantageous electronic stabilization linked to Mn^{2+} (high-spin $3d^5$) within the sulfide lattice. Tc exhibits the highest formation energy (4.45 eV for substitutional and 5.59 eV for interstitial), signifying a greater energetic barrier for incorporation and implying a reduced solubility limit or the necessity for non-equilibrium synthesis conditions [7]. Re demonstrates intermediate E_f, exhibiting formation energies that are lower than Tc but higher than Mn, which aligns with its more delocalized 5d electronic nature. In conclusion, substitutional doping is the energetically preferred method for all examined transition metals. Mn is recognized as the most thermodynamically stable dopant, but Re exhibits stronger stability than Technetium (Tc) despite possessing a larger atomic radius. The findings indicate that substitutional doping can effectively alter the characteristics of $ZnCu_2SnS_4$while preserving structural integrity. Relationship between substitutional formation energies of Mn, Re, and Tc dopants and their qualitative implications for incorporation feasibility in Cu_2SnS_4.

S4 Extended X-ray absorption fine structure (EXAFS)

Fig.S2a presents a comparison of the Fourier-transformed extended X-ray absorption fine structure (EXAFS) ($\chi(R)$), and the corresponding Morlet wavelet transform (WT) contour plots (Fig. S2b) for the M-

S coordination shells in MCu_2SnS_4 (M = Zn, Mn, Tc, Re). All samples display a prominent first-shell peak located between 2.25 and 2.38 Å, affirming tetrahedral M-S coordination in accordance with the kesterite framework. The slight differences in bond lengths (Re-S: 2.256 Å, Tc-S: 2.266 Å, Mn-S: 2.375 Å, Zn-S: 2.368 Å) suggest that the substitution of 3d, 4d, and 5d cations leads to minimal geometric distortion while having a substantial impact on the electronic environment. The WT contour maps demonstrate a systematic evolution in both k and R domains. The Zn-S domain is observed at k ~ 5 $Å^{-1}$ and R ~ 2.2 Å, consistent with the low backscattering amplitude of the 3d absorber. The intensity for Mn–S shifts to k~ 6 $Å^{-1}$, reflecting increased multiple scattering attributed to the higher atomic number (Z = 25). The Tc-S shell exhibits a shift to k~7 $Å^{-1}$, indicating stronger localization, which is characteristic of 4d transition-metal sulphides where photoelectron coherence and scattering amplitude are elevated. The Re-S contribution is distinctly observed at k~9 $Å^{-1}$ and R~2.4 Å, demonstrating the highest WT intensity across all systems. This progression indicates a monotonic increase in the photoelectron backscattering amplitude f(k) and phase shift as the absorber Z increases, demonstrating a shift from covalent Zn-S bonding to more metallic and delocalized Re-S interactions. These trends align with previous WT analyses of transition-metal chalcogenides, which indicated that high-k maxima (8~10 $Å^{-1}$) were linked to heavy 4d/5d absorbers such as Tc and Re. The integrated χ(R) and WT findings present strong evidence that the transition from Zn to Re influences the M-S hybridization strength and local electronic density, which are essential for adjusting charge transfer and catalytic characteristics in multicationic kesterites.

S5 Optical properties

$$\alpha(\omega)=\omega/c[2\varepsilon_2(\omega)/\{\varepsilon_1(\omega)^2+\varepsilon_2(\omega)^2\}^{1/2}]^{1/2} \qquad (1)$$

Fig. S3a and b illustrates the dielectric function and absorption spectra, respectively for $ZnCu_2SnS_4$, $MnCu_2SnS_4$, $TcCu_2SnS_4$, and $ReCu_2SnS_4$, demonstrating the substantial impact of transition-metal substitution on the optical excitation characteristics of Cu_2SnS_4. All doped systems demonstrate significant absorption intensity (~2.5×10^5 cm^{-1}), indicating their superior light-harvesting efficiency over a wide

energy spectrum. The main absorption peaks are observed between 10.39 and 10.92 eV, which are ascribed to interband transitions from the S 3p and Cu/Transition metal d orbitals in the valence band to the Sn 5s/5p and dopant d-states in the conduction band. The systematic blue-shift of the absorption maxima from 10.39 eV (Zn) to 10.84 eV (Mn), 10.87 eV (Tc), and 10.92 eV (Re) demonstrates an increase in optical transition energy associated with heavier dopants. This shift results from enhanced d-p hybridization and relativistic effects in Tc and Re, leading to broader conduction bands and elevated excitation thresholds. The overall intensity increases along the same sequence, indicating the introduction of additional electronic pathways for light-matter interaction because of the partially filled d orbitals. The Re- and Tc-doped systems exhibit the most intense and broad absorption bands, indicating their enhanced capacity to absorb high-energy photons, which align with their elevated dielectric response and metallic-like density of states near the Fermi level. In contrast, $ZnCu_2SnS_4$ exhibits a diminished and slightly red-shifted absorption maximum, indicative of its broader band gap and restricted electronic transitions. The results indicate that transition-metal doping improves optical absorption intensity and transition energy. $TcCu_2SnS_4$ and $ReCu_2SnS_4$ exhibit a favorable combination of strong interband transitions and tunable optical activity, positioning them as promising candidates for optoelectronic and photoresponsive VOC-sensing applications.

S6 Optimized geometries of the VOC adsorbed supercell

The relaxed VOCs (BTD, FA and TCE) adsorbed $ZnCu_2SnS_4$ and Mn, Tc and Re-substituted $ZnCu_2SnS_4$ surfaces established a characteristic of weak physisorption to moderate chemisorption (Fig. S5). BTD adsorption demonstrated a relative distance of 3.268-3.518 Å at all slabs, and this larger distance of the adsorbate away from the surface is attributed to the weak Vander Waals/physisorption with only plausible limited overlap of frontier orbital between BTD and the slab surface. However, the $MnCu_2SnS_4$ system showed the shortest distance of 3.268 Å among all the other slabs. Next, FA results suggest the intermediate distances between ~3.121-3.578 Å consistent with stronger adsorption than BTD for Mn, Tc and Re-based systems because of the presence of the polar C=O functional group, creating an aligned interaction with

metal centres and S atoms of the surfaces. The shortest distance was recorded for the same $MnCu_2SnS_4$ system, reflecting the most favorable surface for the adsorption of FA and BTD, which can be beneficial for the sensing strategy. Compared to other VOCs, TCE exhibited remarkably stronger binding with $TcCu_2SnS_4$, and the shortest distance was 2.308 Å suggests the partial chemisorption or stronger directional binding characteristics of TCE due to its Cl-metal contacts. Overall, the other relaxed TCE adsorbed systems showed longer distances ~3.365-3.562 Å and the longest distance of 3.562 Å has been recorded for the Re-based slab. These relaxed geometries of VOC interacting with slab surfaces depend strongly on the existing functional groups of VOC. These findings suggest Mn-doped Cu_2SnS_4 relatively showed stronger adsorption than other surfaces based on a shorter distance against BTD (3.268 Å) and FA (3.121 Å). The possible reason could be the existence of a high number of electronic states near the Fermi energy level, charge redistribution and induced structural distortions due to Mn-doping collectively expose a larger number of adsorptive sites. On the other hand, the $TcCu_2SnS_4$ system established the shortest distance of 2.308 Å, proving that the Cl-metal interaction could be ascribed to the stronger interaction of TCE.

S7 Charge density difference plot

The charge density difference was calculated by using the following expression: $\Delta\rho=\rho_{VOC\text{-}slab}-\rho_{slab}-\rho_{VOC}$; where, $\rho_{VOC\text{-}slab}$=charge density of VOC adsorbed slab system (Zn, Mn, Tc and Re@Cu_2SnS_4), ρ_{slab}=charge density of slab surface and ρ_{VOC}=charge density of VOC (BTD, FA and TCE). The obtained $\Delta\rho$ plot (Fig. S6 and 2a) contains the yellow and cyan lobes, indicating the charge accumulated and depleted regions of the VOC adsorbed systems. Firstly, the BTD physiosorbed system displayed mostly small, diffused charge density redistribution localization around the molecular π-system and the outer atom surfaces. In brief, the charge accumulation and depletion region is very weak and spread out, which is consistent with the dispersion and weak polarization-driven physisorption. For FA adsorbed systems, it could be seen that the more localized charge redistribution present around the polar group of FA and the surface cations such as Zn, Mn, Tc and Re. In addition, the Mn and Tc systems exhibited the electron depletion of the O atom in

the FA VOC molecule, suggesting the charge transfer and electrostatic stabilization via the carbonyl dipole. TCE adsorption displays a wide range of CDD marks, mainly the $TcCu_2SnS_4$ supercell showed localized charge accumulated and depleted lobes observed at the interface and around Cl atoms, proving the substantial orbital mixing and charge redistribution. While the Δρ plot of other supercells (Zn, Mn and Re) demonstrates a more diffusive and smaller lobes consistent with weaker binding.

S8 Adsorption energy plot

The adsorption energy (E_{ads}) of the individual VOCs was calculated by using the following equation: $E_{ads}=E_{VOC\text{-}slab}-E_{slab}-E_{VOC}$; where, $E_{VOC\text{-}slab}$=Total energy of VOC adsorbed supercell system (112 plane) (Zn, Mn, Tc and Re@Cu_2SnS_4), E_{slab}=Total energy of supercell surface and E_{VOC}=Total energy of VOC (BTD, FA and TCE. The E_{ads} analysis (Fig. 2b) provides insightful information about the sensing characteristics of the transition metal-doped Cu_2SnS_4 supercells. The weakest binding behavior was observed during the BTD interaction (E_{ads}=-0.232 to -0.334 eV), corresponding to the weak physisorption with low charge transfer, indicating the low sensitivity but remarkable reversibility for a BTD sensor, possibly. On the contrary, FA demonstrates moderate E_{ads} for $MnCu_2SnS_4$ (-0.49 eV), suggesting the partial chemisorption driven by dipole-surface interactions. The moderate binding characteristic could be helpful for the efficient adsorption and desorption process during the sensing strategy, potentially an ideal candidate which facilitates highly selective and reversible detection of FA molecule. The E_{ads} plot shows that the strongest binding energy was observed at TCE adsorbed $TcCu_2SnS_4$, which is in good agreement with the shortest bonding distance of 3.009 Å and the obvious charge density differences at the interface of the TCE-Tc supercell system. The largest E_{ads} value suggests the partial chemisorption and significant orbital overlap that could be facilitating higher selectivity, but slower and moderate reversibility. Ultimately, as per the above findings $MnCu_2SnS_4$ system could be a promising and effective catalyst for VOC sensing with remarkable reversibility; however, the $TcCu_2SnS_4$ catalyst can provide a greater number of adsorptive sites for chlorinated VOCs.

S9 NEB analysis

The minimum energy pathways (Fig. 3) derived from CI-NEB calculations validate the Mn and Tc dopant-dependent VOC sensing behaviour of Cu_2SnS_4. In the case of $MnCu_2SnS_4$, BTD and formaldehyde (FA) demonstrate lower adsorption transition barriers of 0.009 eV and 0.070 eV, respectively, indicating a rapid and kinetically favorable physisorption process (Fig. S7). The final states are approximately 0.18-0.22 eV lower in energy than the initial states, which aligns with the previously observed moderate binding energies and short adsorption distances. The minimal barriers suggest that Mn-based Cu_2SnS_4 surfaces facilitate rapid adsorption-desorption cycling, which is essential for reversible VOC sensing. The adsorption of trichloroethylene (TCE) on $MnCu_2SnS_4$ occurs with a barrier of 0.138 eV, indicating a more directional interaction characterized by Cl-Metal contacts. The interaction of the same VOC with $TcCu_2SnS_4$ results in a barrier increase to 0.174 eV, while the pathway becomes more exergonic, consistent with its enhanced binding energy and greater charge redistribution. This kinetic preference supports the previously inferred trend of chemical selectivity. Mn-doped surfaces facilitate rapid and reversible detection of non-chlorinated VOCs (BTD, FA), while Tc-doped Cu_2SnS_4 is remarkable for the strong and partially irreversible capture of chlorinated VOCs like TCE. The Mn system, characterized by the highest ZT and manipulated d-band alignment near the Fermi level, facilitates low-barrier, and reversible sensing. In contrast, the metallic Tc system combines high conductivity with enhanced adsorption kinetics, resulting in selectivity but reduced reversibility. The results confirm that d-band engineering concurrently adjusts thermoelectric efficiency, adsorption energetics, and reaction kinetics, facilitating the rational alignment of doped Cu_2SnS_4 surfaces with specific VOC classes.

S10 Plane-averaged electrostatic potential

Fig. S9a shows the plane-averaged electrostatic potential profile for pristine Transition metal-doped Cu_2SnS_4 and after VOC adsorption at corresponding supercells. The work function (Φ) value was calculated from the difference between the vacuum and Fermi level. The small dip in the plane-averaged electrostatic potential is caused by the localized dipole generated by the charge redistribution upon the adsorption of adsorbates. The observed Φ values for the clean slab surface ranged from 3.40 to 2.83 eV, indicating the electronic state enhancement from Zn to Re has greatly influenced the electrostatic potential. It is known that the decreasing Φ values cause the slab surface to be rich in electrons. Specifically, 4d and 5d transition-metal doping decreases the surface potential barrier because of their charge redistribution and delocalized electronic states. Upon VOC adsorption, a substantial shift in the Φ value has been noted, suggesting the signifying charge transfer between the adsorbate and substrate. On $ZnCu_2SnS_4$, the Φ value increased from 3.40 to 3.46 (BTD) and 3.43 eV (FA) (Fig. S9b). A slight increase in the Φ denotes the electron donation to the adsorbate (BTD and FA) VOC. In contrast, TCE adsorbed $ZnCu_2SnS_4$ showed a decreased Φ, which demonstrates the electron acceptance of the slab surface from TCE. For the $MnCu_2SnS_4$ system, the Φ value has been shifted to 3.02 and 2.99 eV for BTD and TCE, respectively (Fig. S9c). A small decrement in the Φ signifies the electron-rich surface due to the acceptance of electrons from BTD and TCE. On the other hand, a drastic increase in Φ from 3.05 to 4.68 eV indicates the strong electron withdrawal from the substrate to FA. In $TcCu_2SnS_4$, Φ changes to 2.80 (BTD) and 2.83 eV (TCE) from 2.91 eV, but a slight increase in Φ was observed upon FA adsorption (Fig. S9d). The Tc-based system established a stronger binding for TCE; however, ΔΦ is very low due to the strong bonding characteristics, charge redistribution does not affect it altogether, and the narrow band gap of the Tc system, which exhibits the metallic nature, caused no shift in the Fermi energy level. For $ReCu_2SnS_4$, Φ becomes 2.75 eV (TCE), 2.88 eV (FA), and 3.02 eV (BTD), with reasonable shifts indicating mixed charge-transfer characteristics (Fig. S9e) .

S11 Density of states

The displayed projected density of states (PDOS) plots (Fig. S10) illustrates the orbital-level interactions between the adsorbates (BTD, FA, and TCE) and the transition-metal-doped Cu_2SnS_4 surfaces (Zn, Mn, Tc, Re). The s, p, and d states of the adsorbate and surface across all systems display unique hybridization patterns, elucidating the electronic basis of adsorption strength and selectivity. In $ZnCu_2SnS_4$, the valence s and p states of the adsorbates are distinctly separated from the conduction region, exhibiting minimal overlap near the Fermi level. This observation confirms that the interaction is predominantly physisorption, attributed to the deep-lying Zn 3d orbitals. In contrast, $MnCu_2SnS_4$ exhibits significant s-p-d hybridization in the energy range of -4 to 0 eV, especially during FA adsorption, where there is a strong mixing of Mn 3d and O 2p orbitals. This interaction contributes to the substantial increase in work function and notable charge transfer. The $TcCu_2SnS_4$ system demonstrates substantial orbital coupling, with the adsorbate p and Tc 4d states creating continuous electronic features at the Fermi level. This is indicative of metallic-like hybridization, which accounts for its elevated adsorption energies, particularly for TCE. $ReCu_2SnS_4$ exhibits moderate and extensive d-orbital participation, indicating a balanced interaction between chemisorption and physisorption that stabilizes the adsorbed species while minimizing significant Fermi-level distortion. The enhancement of adsorbate–substrate orbital overlap from Zn to Mn, Re, and Tc is directly correlated with increased adsorption strength. This relationship confirms that stronger s/p-d orbital hybridization near the Fermi level is fundamental to the enhanced electronic coupling and charge transfer efficiency observed in the Tc-doped surface, establishing it as the most reactive system for TCE detection.

S12 Thermoelectric properties

Seebeck coefficient

$$S_{\alpha\beta}(T,\mu) = \frac{1}{eT\Omega\sigma_{\alpha\beta}(T,\mu)} \int \sigma_{\alpha\beta}(\varepsilon)\,(\varepsilon-\mu) - \left[\frac{\delta f_0(T,\varepsilon,\mu)}{\delta\varepsilon}\right] d\varepsilon \quad (2)$$

$S_{\alpha\beta}(T,\mu)$: Seebeck coefficient tensor component along directions α and β; T: Absolute temperature; μ: Chemical potential; e: Elementary charge; Ω: Unit-cell volume; $\sigma_{\alpha\beta}(T,\mu)$: Electrical conductivity tensor; $\sigma_{\alpha\beta}(\varepsilon)$: Energy-resolved conductivity tensor; ε: Carrier energy; $f_0(T,\varepsilon,\mu)$: Fermi-Dirac distribution function; $\frac{\partial f_0}{\partial\varepsilon}$: Energy derivative of the Fermi-Dirac distribution.

Electrical conductivity

$$\sigma_{\alpha\beta}(T,\mu) = \frac{1}{\Omega} \int \alpha_{\alpha\beta}(\varepsilon) - \left[\frac{\delta f_0(T,\varepsilon,\mu)}{\delta\varepsilon}\right] d\varepsilon \quad (3)$$

$\sigma_{\alpha\beta}(T,\mu)$: Electrical conductivity tensor component;

Electrical thermal conductivity

$$\kappa_{\alpha\beta}(T,\mu) = \frac{1}{e^2T\Omega} \int \sigma_{\alpha\beta}(\varepsilon)\,(\varepsilon-\mu)^2 - \left[\frac{\delta f_0(T,\varepsilon,\mu)}{\delta\varepsilon}\right] d\varepsilon \quad (4)$$

$\kappa_{\alpha\beta}(T,\mu)$: Electronic thermal conductivity tensor component along directions $\alpha$and βT: Absolute temperature; μ: Chemical potential; e: Elementary charge; $\sigma_{\alpha\beta}(\varepsilon)$: Energy-resolved electrical conductivity tensor; ε: Carrier energy; $(\varepsilon-\mu)^2$: Square of the energy deviation from the chemical potential;

Power factor

$$PF_{\alpha\beta}(T,\mu) = S^2{}_{\alpha\beta}(T,\mu) \cdot \sigma_{\alpha\beta}(T,\mu) \quad (5)$$

$PF_{\alpha\beta}(T,\mu)$: Powern factor along directions α and β;

Figure of merit

$$ZT_{\alpha\beta}(T,\mu) = \frac{S^2{}_{\alpha\beta}(T,\mu) \cdot \sigma_{\alpha\beta}(T,\mu) \cdot T}{\kappa_{\alpha\beta}(T,\mu) + \kappa_{l,\alpha\beta}(T,\mu)} \quad (6)$$

$ZT_{\alpha\beta}(T,\mu)$: Dimensionless thermoelectric figure of merit tensor component along directions $\alpha$and β; $S_{\alpha\beta}(T,\mu)$: Seebeck coefficient tensor; $S^2_{\alpha\beta}(T,\mu)$: Square of the Seebeck coefficient; $\sigma_{\alpha\beta}(T,\mu)$: Electrical conductivity tensor; $\kappa_{\alpha\beta}(T,\mu)$: Electronic thermal conductivity tensor; $\kappa_{l,\alpha\beta}(T,\mu)$: Lattice (phonon) thermal conductivity tensor; μ: Chemical potential

The Seebeck plot (Fig. S11a) illustrate the varying impacts of each dopant on charge transport in Cu_2SnS_4 [8]. At 300 K, Zn-doped Cu_2SnS_4 exhibits a Seebeck coefficient of –37.02 μV K^{-1} near E-E_F=0 region, indicating n-type behaviour due to the electron donation from Zn. Mn, Tc, and Re-doped samples exhibit positive Seebeck coefficients of +124.88 μV K^{-1}, +13.89 μV K^{-1}, and +74.69 μV K^{-1}, respectively, indicating predominant hole conduction (p-type). Mn exhibits the highest thermopower among the four, whereas Tc demonstrates the lowest positive response. The significant rise in Seebeck magnitude at altered energy levels for Mn and Zn indicates the substantial impact of these dopants on state asymmetry in proximity to the Fermi level.

The electrical conductivity (Fig. S11b) of Cu_2SnS_4 exhibits a significant variation based on the dopant, indicating the influence of each metal on the material's transport properties. At 300 K, Zn-doped CTS exhibits a conductivity of 5.40×10^{18} Ω^{-1} m^{-1} s^{-1}, which underscores its semiconducting characteristics and restricted charge carrier mobility. Replacing Zn with Mn results in a modest increase in conductivity to 6.90×10^{18} Ω^{-1} m^{-1} s^{-1}, attributed to the introduction of 3d states that improve carrier delocalisation. The effect is significantly enhanced with Re and Tc doping: Re-doped CTS achieves a conductivity of 4.29×10^{19} Ω^{-1} m^{-1} s^{-1}, while Tc doping elevates conductivity

to 1.03×10^{20} Ω^{-1} m^{-1} s^{-1}, indicating the emergence of metallic-like behaviour attributed to substantial 4d/5d orbital overlap. This sequence from Zn to Mn to Re to Tc demonstrates a distinct transition from semiconducting to quasi-metallic transport, which is a crucial factor in optimizing sensitivity, response time, and conductivity in VOC sensing devices.

At 300 K, the electronic contribution to thermal conductivity (κ) (Fig. S11c) demonstrates a distinct dependence on the dopant used. $ZnCu_2SnS_4$ crystal exhibits a thermal conductivity of 4.11×10^{13} W m^{-1} K^{-1} s^{-1}, indicative of its semiconducting properties and reduced carrier mobility. Mn doping approximately doubles the value to 8.07×10^{13} W m^{-1} K^{-1} s^{-1}, which aligns with the enhanced electron delocalization from its 3d orbitals. A significant increase is noted for the substitutions of Tc and Re: $TcCu_2SnS_4$ attains a value of 7.08×10^{14} W m^{-1} K^{-1} s^{-1}, which is nearly an order of magnitude greater than that of Mn, whereas $ReCu_2SnS_4$ exhibits a value of 3.36×10^{14} W m^{-1} K^{-1} s^{-1}. This progression corresponds to the improved metallic-like carrier response from the extended 4d and 5d orbitals of Tc and Re, which enhances free-electron transport and, consequently, κ. In sensing applications, increased thermal conductivity can diminish baseline noise and facilitate quicker thermal equilibration; however, it may concurrently decrease the thermal gradient essential for thermoelectric transduction.

At the Fermi level, $ZnCu_2SnS_4$ exhibits a minimal power factor (Fig. S11d) of 7.40×10^{9} W m^{-1} K^{-2} s^{-1}, aligning with its reduced Seebeck response and diminished electrical conductivity. Replacing Zn with Mn significantly enhances the power factor to 1.08×10^{11} W m^{-1} K^{-2} s^{-1}, attributed to the substantial positive Seebeck coefficient (+124.88 μV K^{-1}) and a moderate increase in conductivity. $TcCu_2SnS_4$ demonstrates a moderate value of 1.98×10^{10} W m^{-1} K^{-2} s^{-1}, which reflects a trade-off between a lower Seebeck coefficient and enhanced electrical conductivity. The maximum power factor is achieved for $ReCu_2SnS_4$, attaining 2.39×10^{11} W m^{-1}

K^{-2} s^{-1}, signifying the most efficient interaction between charge transport and thermoelectric response across all doped systems. The sequence $ZnCu_2SnS_4$ < $TcCu_2SnS_4$ < $MnCu_2SnS_4$ < $ReCu_2SnS_4$ reflects the increasing enhancement of d-p orbital hybridization, indicating that Re is the most effective dopant for optimizing thermoelectric power output, whereas Mn offers a viable option with a high-power factor and diminished electronic thermal losses.

The transition metals-doped Cu_2SnS_4 materials exhibit a definite advantage in thermoelectric performance at 300 K (Fig. S11e). $MnCu_2SnS_4$ exhibits the highest ZT value of 0.400, attributed to its advantageous combination of a high Seebeck coefficient, good electrical conductivity, and relatively low thermal conductivity. $ReCu_2SnS_4$ exhibits a ZT of 0.214, primarily influenced by its robust power factor, although it is somewhat constrained by thermal leakage. $ZnCu_2SnS_4$ has a value of 0.054, indicating its relatively modest electronic properties and reduced carrier mobility. $TcCu_2SnS_4$ exhibits high conductivity and power factor; however, it attains a ZT value of only 0.008 due to its elevated thermal conductivity, which facilitates excessive heat dissipation and diminishes overall thermoelectric efficiency. Mn substitution represents a promising approach to improving ZT in this material family at room temperature. In contrast, Tc doping may be more appropriate for high-conductivity applications where heat retention is less significant.

The thermoelectric trends strongly suggest the VOC sensing mechanism. $MnCu_2SnS_4$, with the highest ZT (0.400 at 300 K), also shows strong yet reversible binding with BTD and FA ideal for selective sensing. In contrast, the metallic, high-conductivity $TcCu_2SnS_4$ has the lowest ZT but exhibits a stronger affinity toward TCE. These correlations indicate that ZT can serve as a predictive descriptor for tuning Cu_2SnS_4-based materials toward target-specific VOC detection.

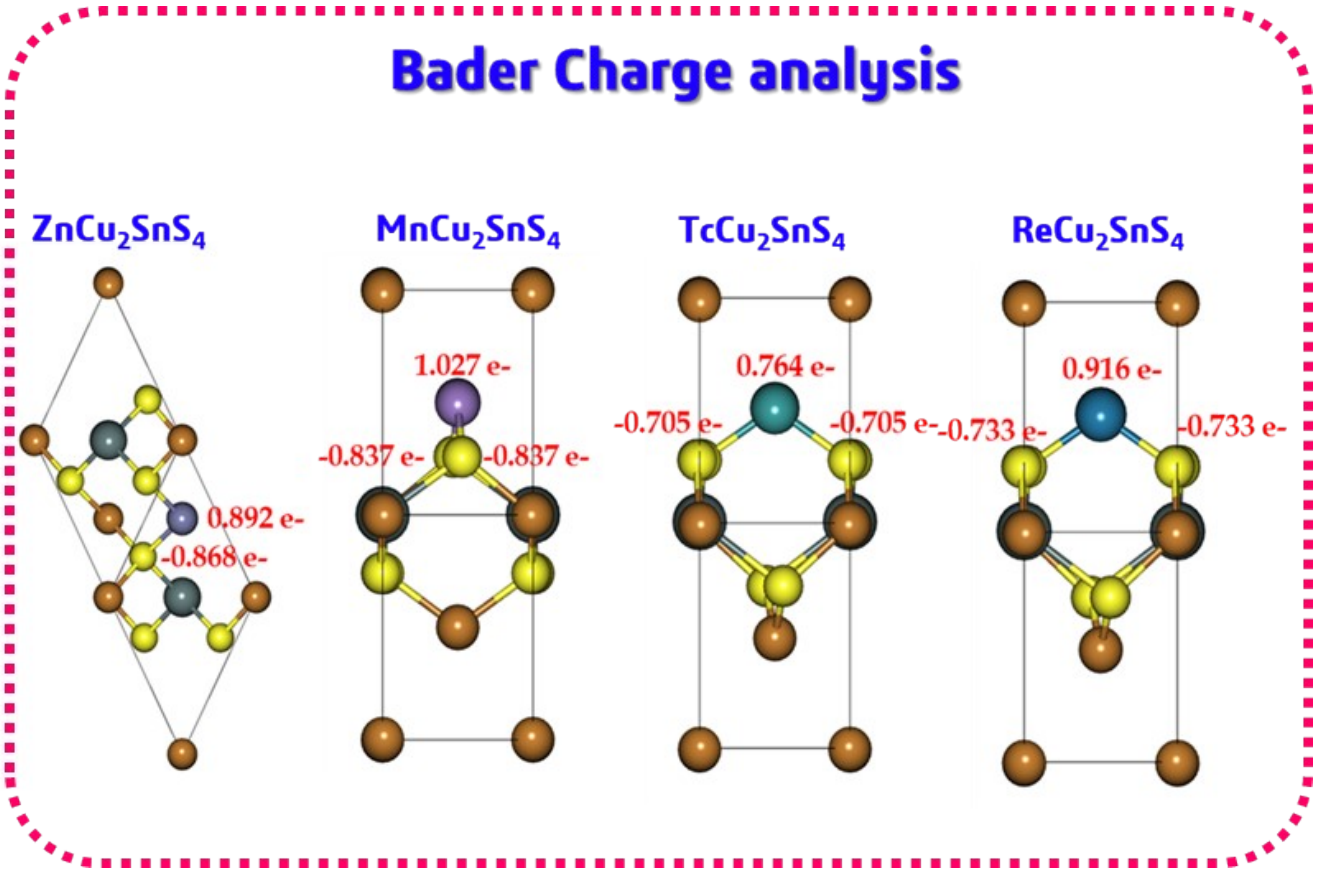

Fig. S1 Bader charge distributions illustrate the increasing metal-S covalency and charge transfer resulting from doping.

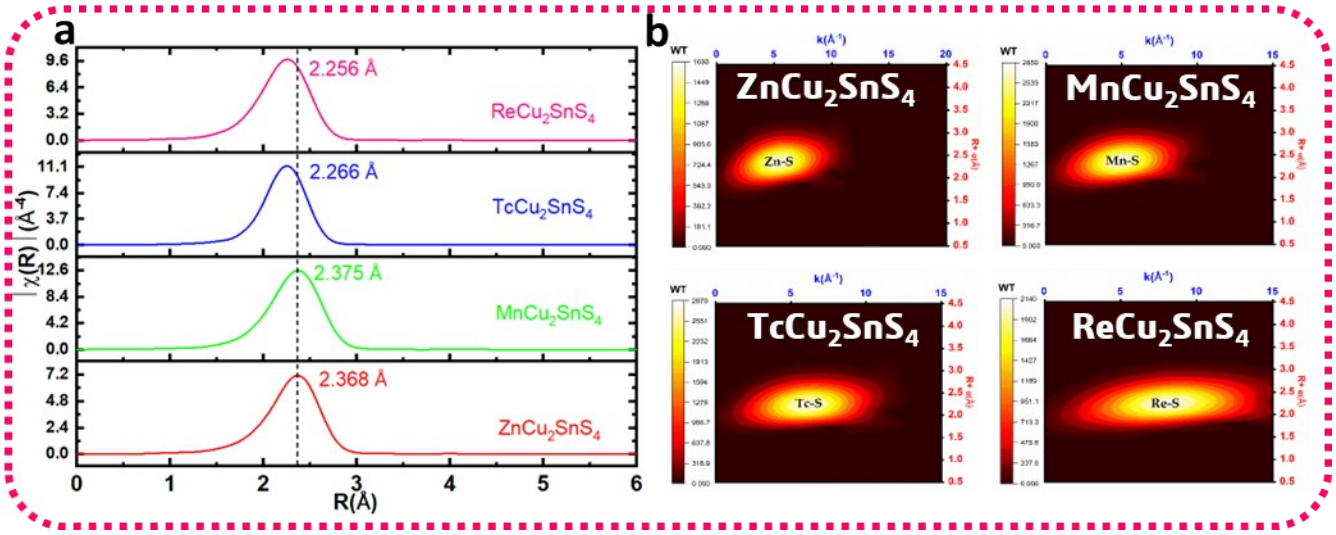

Fig. S2 Fourier-transformed EXAFS of radial distance plot indicates a coordination shortening of metal-S from Mn to Zn to Tc to Re, and (j) Morlet wavelet transform maps indicate an increase in backscattering intensity with the substitution from 3d to 4d to 5d.

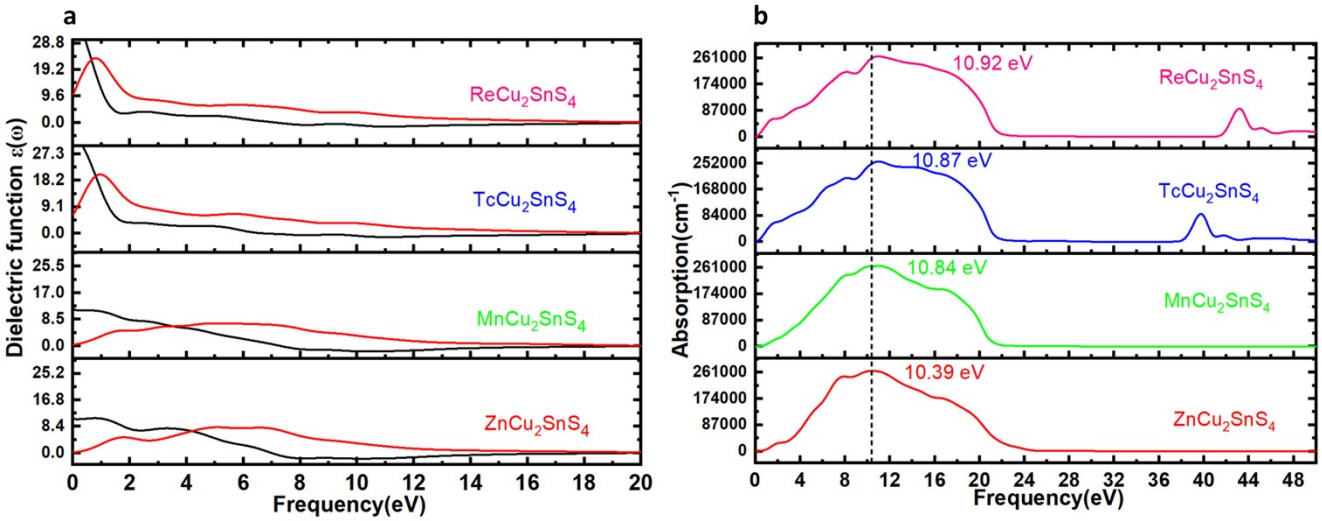

Fig. S3 Frequency (eV)-dependent (a) dielectric function and (b) absorption spectra of Zn-, Mn-, Tc- and Re-doped Cu_2SnS_4. Doping gradually boosts low-energy dielectric response and blue-shifts the characteristic absorption peak from 10.39 eV (Zn) to 10.92 eV (Re).

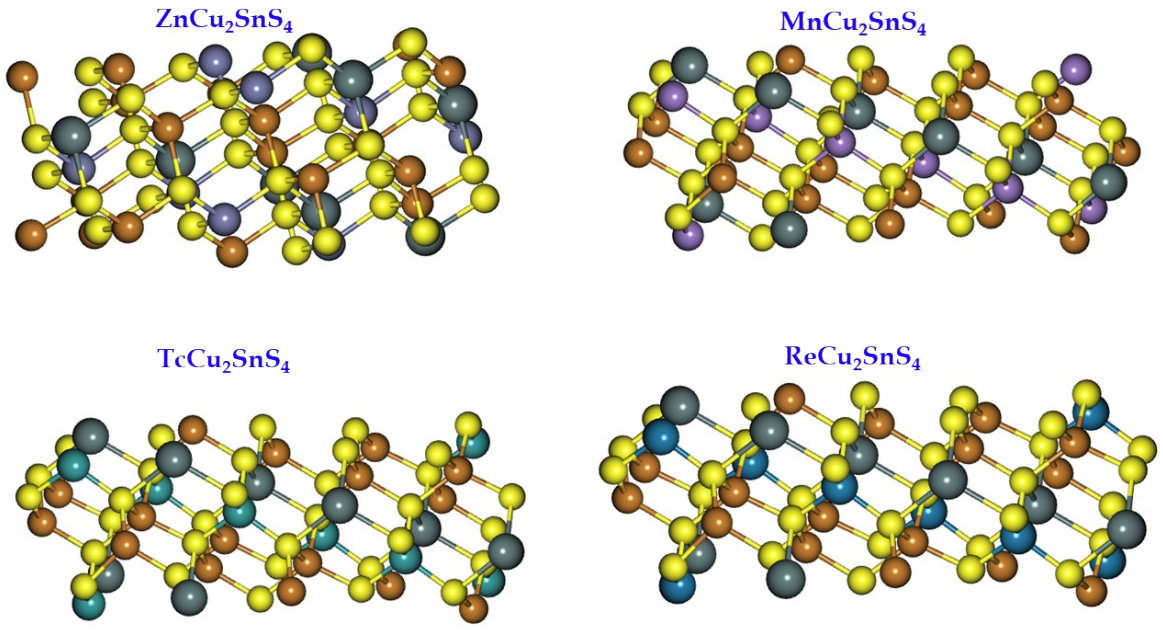

Fig. S4 Geometry-optimized 2×2×1 Cu_2SnS_4 supercells with Zn, Mn, Tc, and Re substitution.

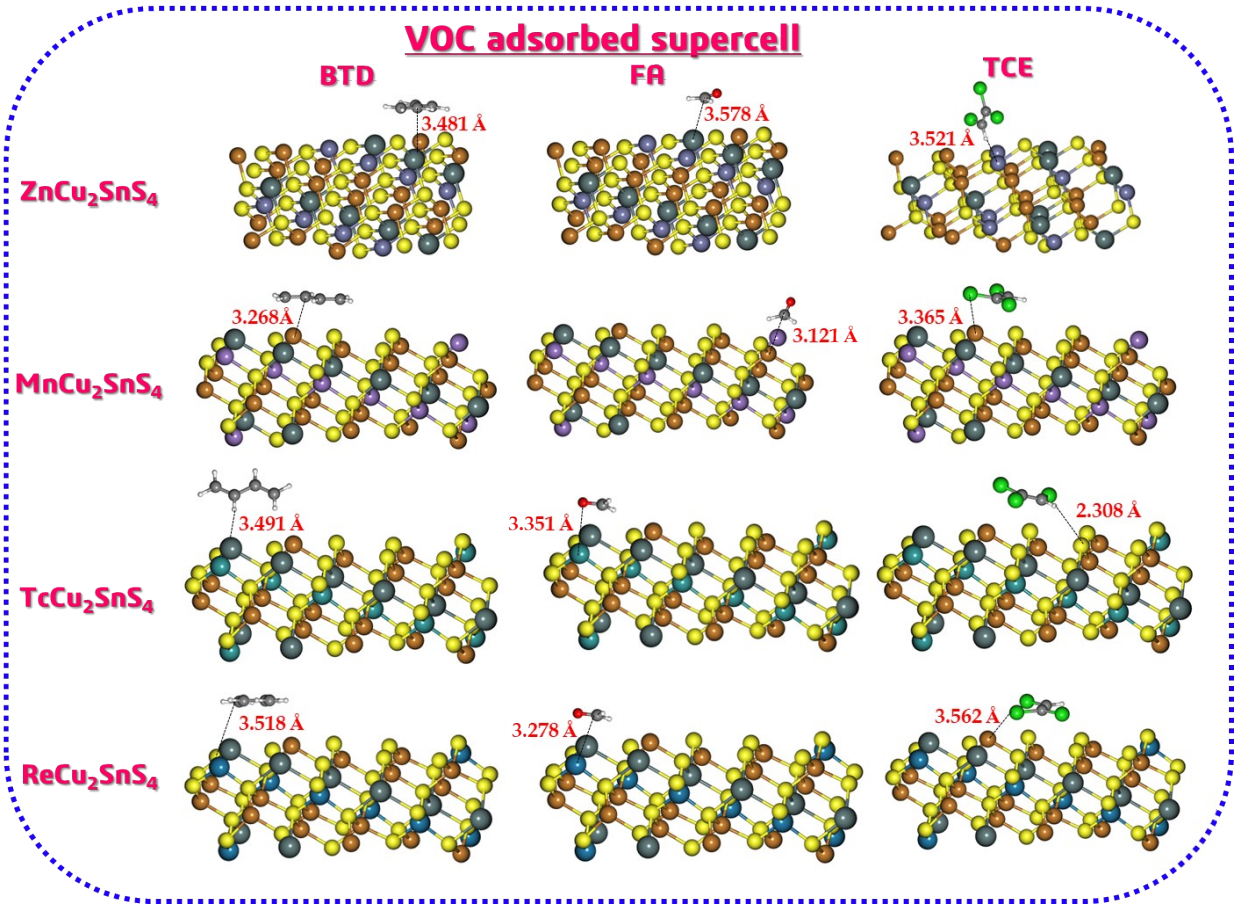

Fig. S5 DFT-relaxed 2×2×1 supercells of Zn-, Tc-, and Re-doped Cu_2SnS_4 with adsorbed VOCs (BTD, FA, TCE). The shortest distance between the supercell and the corresponding nearby atoms of VOC molecule has been reported in Å.

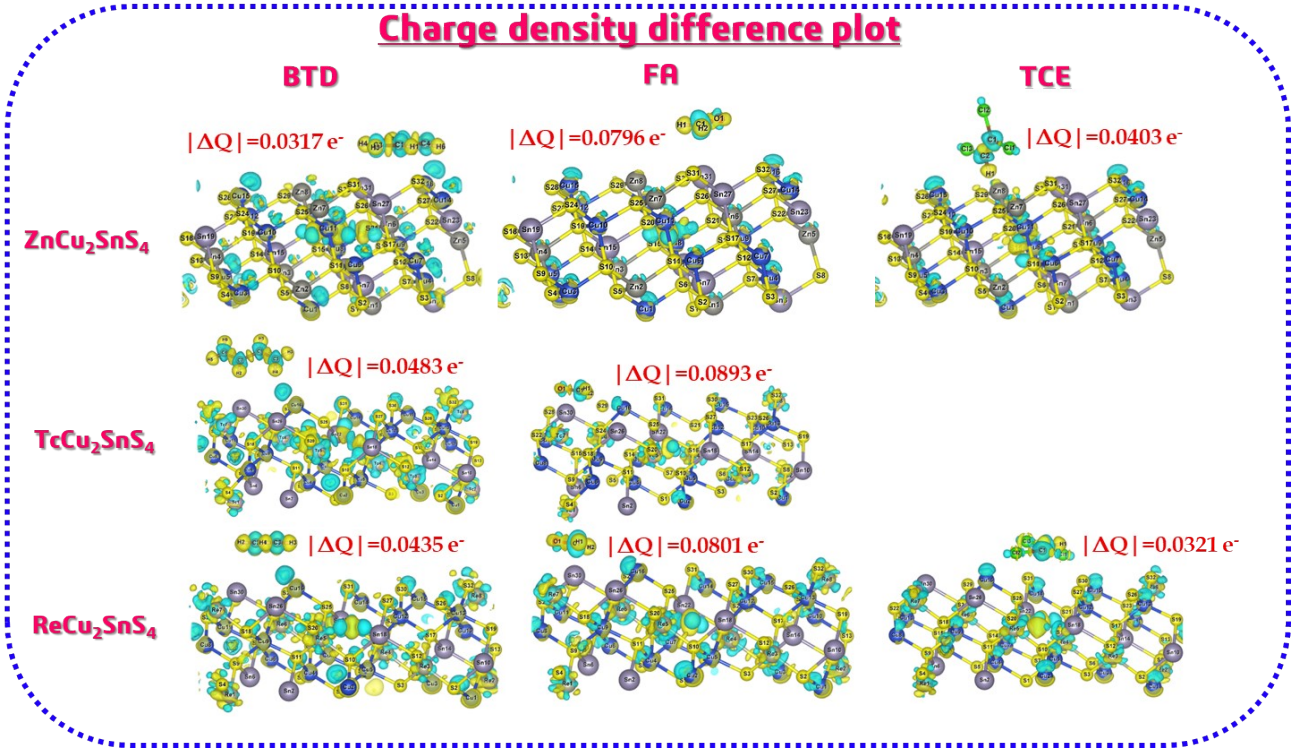

Fig. S6 Charge density difference (Δρ) plots for BTD, FA, and TCE adsorption on Zn-, Tc-, and Re-substituted Cu_2SnS_4 surfaces. Yellow and cyan isosurfaces represent charge accumulation and depletion region, respectively.

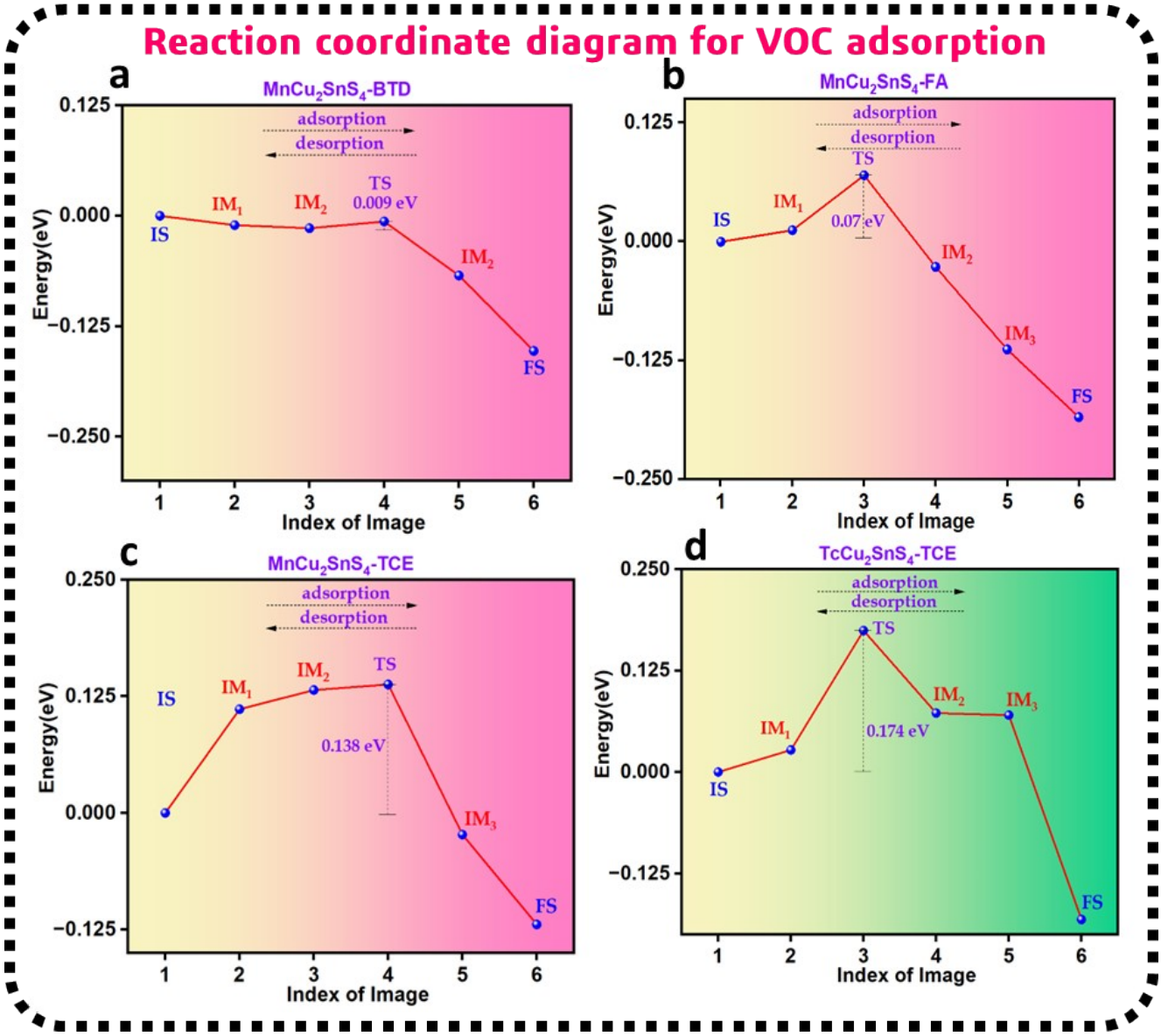

Fig. S7 Reaction coordinate diagrams for VOC adsorption on Mn- and Tc-doped Cu_2SnS_4 surfaces. Optimized states (initial state (IS) to transition state (TS) and TS to final state (FS)) for (a) BTD, (b) FA and (c) TCE adsorption on $MnCu_2SnS_4$, and (d) TCE adsorption on $TcCu_2SnS_4$, showing ultralow barriers for BTD (0.009 eV) and FA (0.070 eV) on $MnCu_2SnS_4$, indicating fast and reversible physisorption, while TCE shows a higher barrier (0.174 eV) and stronger exergonic binding on $TcCu_2SnS_4$, confirming selective and partially irreversible chemisorption.

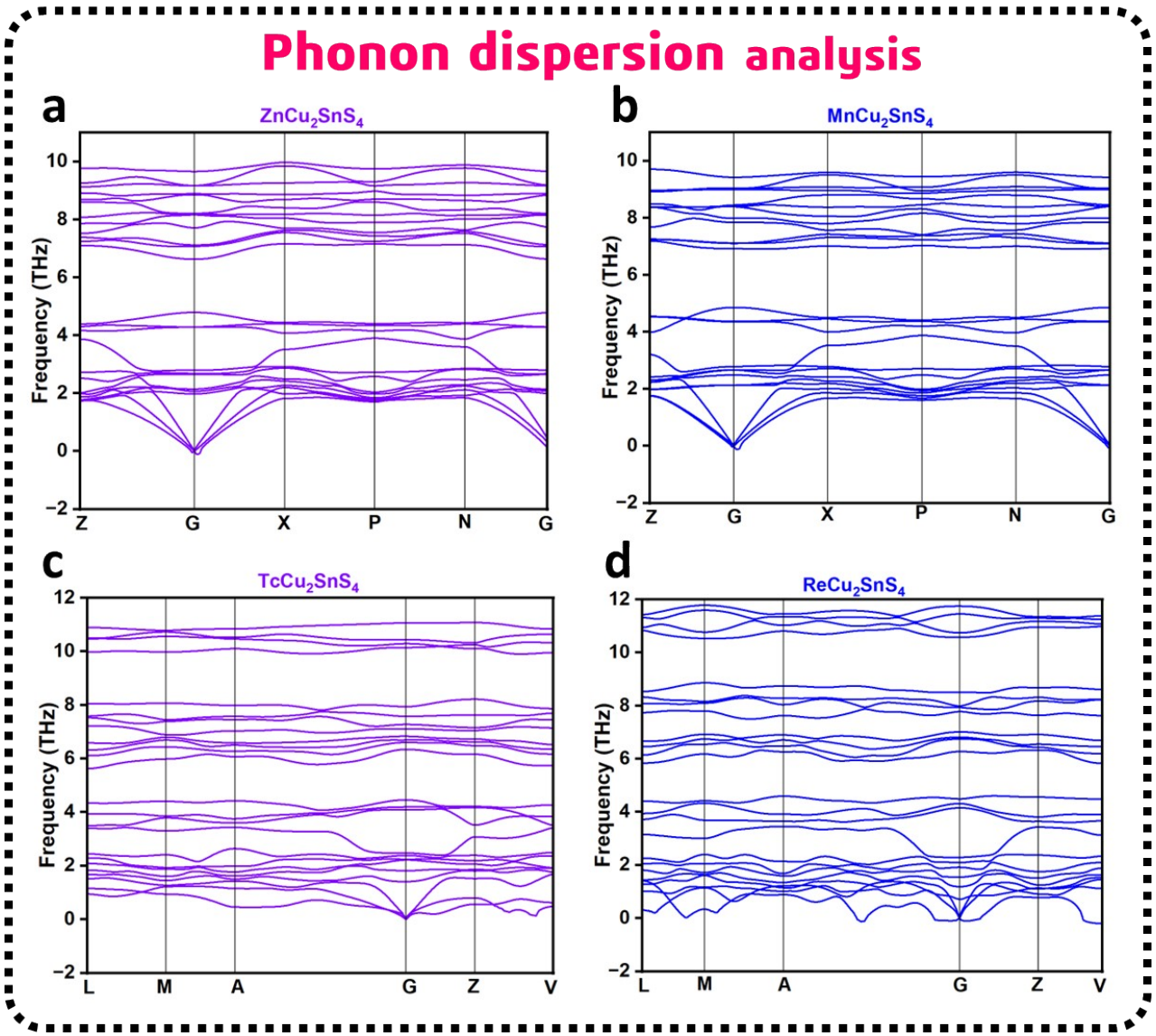

Fig. S8 Phonon band structures of (a) $ZnCu_2SnS_4$, (b) $MnCu_2SnS_4$, (c) $TcCu_2SnS_4$, and (d) $ReCu_2SnS_4$ calculated along the high-symmetry paths of the Brillouin zone. The absence of imaginary phonon frequencies across the entire Brillouin zone confirms the dynamical stability of all crystals. Minor softening of low-frequency acoustic modes in the doped systems originates from finite supercell effects and does not indicate structural instability.

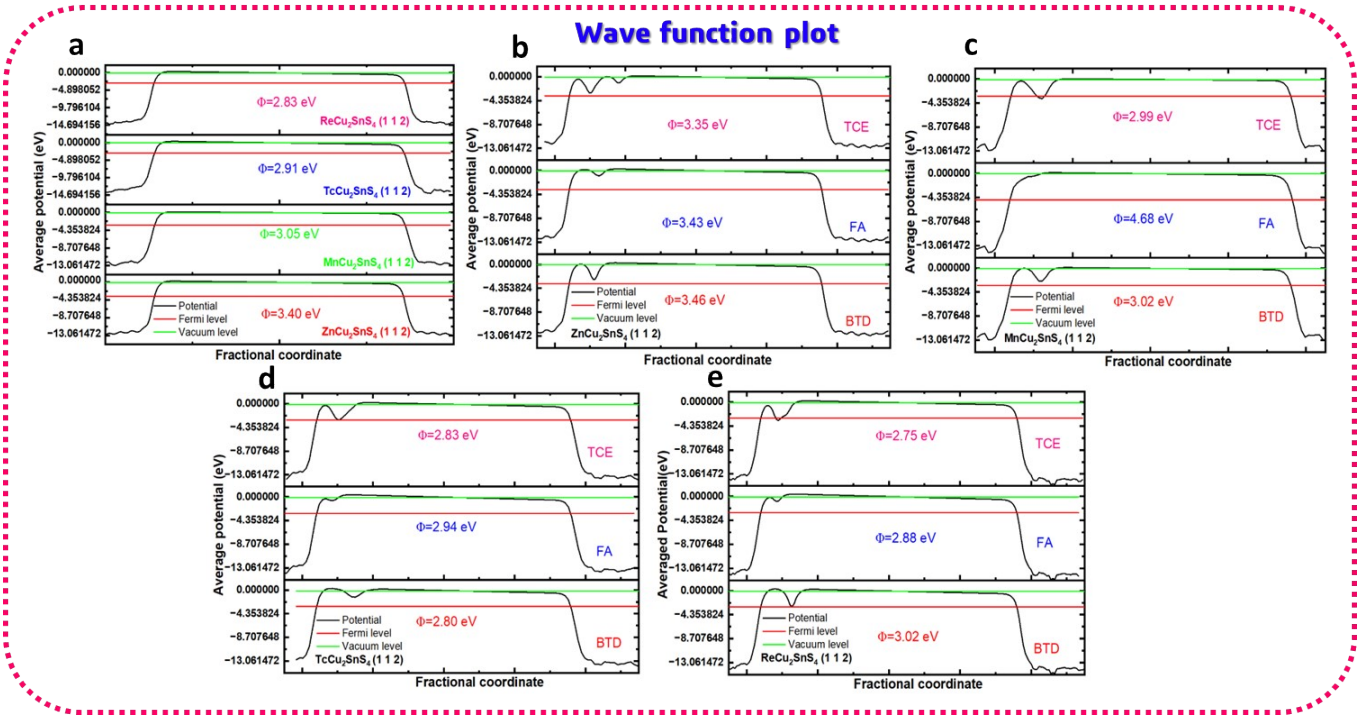

Fig. S9 (a) Plane-averaged electrostatic potential profiles for Zn, Mn, TC, and Re-doped Cu_2SnS_4 , and work-function (Φ) plots of BTD, FA, and TCE adsorbed on (b) Zn, (c) Mn, (d) Tc, and (e) Re-doped Cu_2SnS_4 (112) surfaces. The Fermi level, vacuum level, and corresponding work function (Φ) are indicated, demonstrating VOC-dependent shifts in surface dipole and electronic alignment.

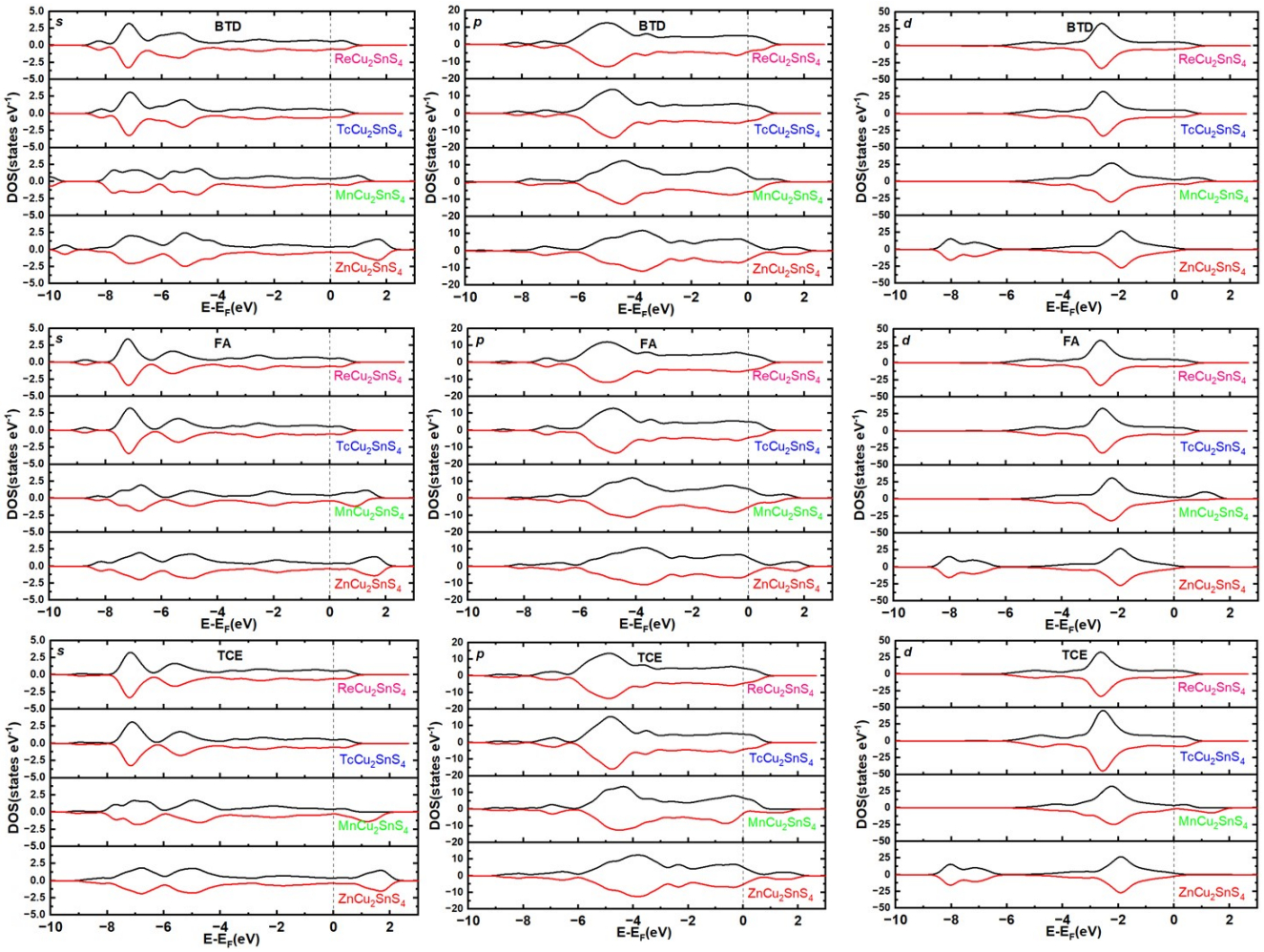

Fig. S10 Spin-polarized projected DOS (s, p, d) of Zn-, Mn-, Tc-, and Re-doped crystals after adsorption of BTD, FA, and TCE. Black and red curves correspond to spin-up and spin-down DOS channels referenced to the Fermi level ($E-E_F= 0$ eV).

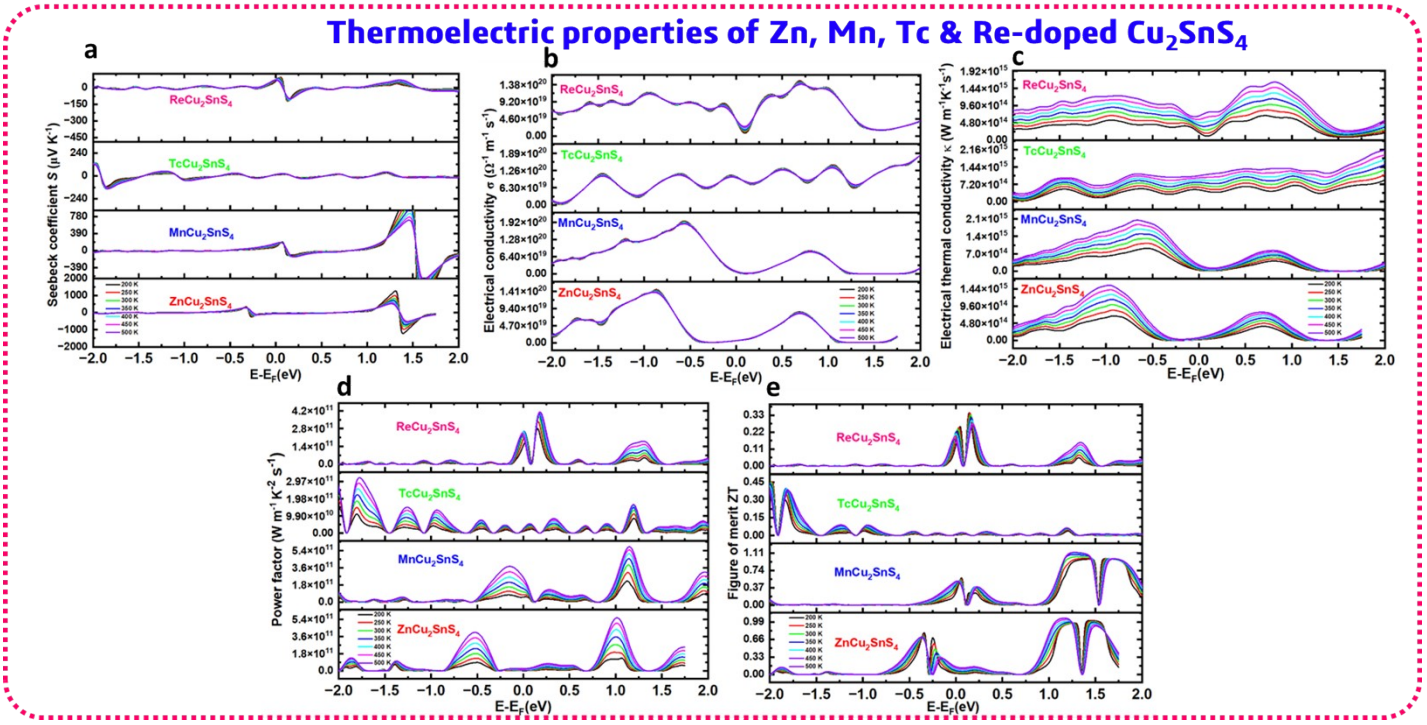

Fig. S11 Thermoelectric transport properties of Zn-, Mn-, Tc- and Re-doped Cu_2SnS_4 as a function of carrier energy at different temperatures: (a) Seebeck coefficient S, (b) electrical conductivity (σ/τ), (c) electronic thermal conductivity (κ_e/τ), (d) power factor ($S^2\sigma/\tau$), and (e) thermoelectric figure of merit (ZT) and $MnCu_2SnS_4$ shows the highest room-temperature ZT, while $TcCu_2SnS_4$ exhibits metallic-like conductivity with suppressed ZT due to enhanced electronic thermal conductivity.

Table. S1 List of Group 1 carcinogenic volatile organic compounds reported by WHO/IARC.

Compound	IARC Classification (2024)	WHO / WHO-Aligned Guideline or Reference Concentration	Averaging Period / Basis	Primary Health Endpoint
1,3-Butadiene(BTD)	Group 1	No threshold; risk-based ~ 2–3 $\mu g \cdot m^{-3}$ (annual mean) for ~10^{-5} risk (WHO-aligned)	Annual	Leukemia/lymphoma
Formaldehyde(FA)	Group 1	100 $\mu g \cdot m^{-3}$ (0.1 $mg \cdot m^{-3}$) 30-min indoor guideline (WHO 2010)	30 min	Nasopharyngeal cancer; mucosal irritation
Trichloroethylene (TCE)	Group 1	~ 2 $\mu g \cdot m^{-3}$ (annual mean) risk-based (WHO/EU aligned)	Annual	Kidney cancer; hepatotoxicity

Table. S2 Monkhorst–Pack k-point grid convergence test

System	Monkhorst–Pack grid	Total energy (eV)	Energy difference ($\lvert E \rvert$, meV)
$ZnCu_2SnS_4$	6 × 6 × 8	-5853.656617942	0.00213
	8 × 8 × 10	-5853.656621186	0.00111
	10 × 10 × 12	-5853.656620075	0.00000
	12 × 12 × 14	-5853.656620188	0.00011
$MnCu_2SnS_4$	6 × 6 × 8	-4816.318019296	0.09585
	8 × 8 × 10	-4816.317942619	0.01917
	10 × 10 × 12	-4816.317923450	0.00000
	12 × 12 × 14	-4816.317917823	0.00563
$TcCu_2SnS_4$	6 × 6 × 8	-6369.280468663	0.75346
	8 × 8 × 10	-6369.292047620	12.33241
	10 × 10 × 12	-6369.279715207	0.00000
	12 × 12 × 14	-6369.279912948	0.19774
$ReCu_2SnS_4$	6 × 6 × 8	-6620.597298435	0.66692
	8 × 8 × 10	-6620.582160071	14.47144
	10 × 10 × 12	-6620.596631515	0.00000
	12 × 12 × 14	-6620.596552866	0.07865

Table. S3 Interstitial and substitutional doping evaluation

Method of doping	System	Total energy (eV)	E_f (eV)
Interstitial doping	$MnZnCu_2SnS_4$	-6506.005957722	3.223585310
	$TcZnCu_2SnS_4$	-8059.398484063	5.586579768
	$ReZnCu_2SnS_4$	-8310.177690796	5.017559466
Substitutional doping	$MnCu_2SnS_4$	-4816.31792345	1.653740429
	$TcCu_2SnS_4$	-6369.279715207	4.447469472
	$ReCu_2SnS_4$	-6620.596631515	3.340739595

Table S4 Possible synthesis routes of Mn, Tc and Re-doped systems according to their thermodynamic rationale

Dopant	Synthesis route	Thermodynamic rationale
Mn	Solution-based methods (sol-gel, spin-coating)	The low substitutional formation energy (E_f = 1.65 eV) suggests straightforward integration under near-equilibrium circumstances, which favours homogeneous substitution at moderate processing temperatures [9].
Re	Hydrothermal or sputtering-based routes	The elevated formation energy (E_f = 3.34 eV) indicates a greater energetic barrier for substitution, necessitating improved kinetic control or increased processing energy to facilitate lattice integration [10].
Tc	Physical deposition routes (co-sputtering)	The elevated substitutional formation energy (E_f = 4.45 eV) suggests restricted equilibrium solubility, signifying that non-equilibrium or high-energy synthesis methods are necessary to surpass thermodynamic limitations [11].

System	C1	C2	C3	C4	H1	H2	H3	H4	H5	H6
$ZnCu_2SnS_4$ BTD	-0.0296	0.0117	-0.0483	-0.12	0.0305	0.007	0.0369	0.0239	0.0183	0.0378
BTD only	-0.0333	-0.0035	-0.096	-0.1213	0.0316	0.0255	0.043	0.0417	0.0695	0.0427
$MnCu_2SnS_4$ BTD	-0.0543	-0.003	-0.0723	-0.0888	-0.0454	0.0419	0.0876	0.0492	0.0414	-0.0263
BTD only	-0.0329	-0.0271	-0.0869	-0.0712	0.002	0.0334	0.0855	0.0256	0.039	0.0327
$TcCu_2SnS_4$ BTD	-0.0095	-0.0434	-0.0512	-0.0731	0.0177	0.0206	0.0058	0.0101	0.0492	0.0261
BTD only	0.0072	0.0098	-0.0328	-0.0639	0.0051	0.0272	-0.0058	0.0175	0.0287	0.0076
$ReCu_2SnS_4$ BTD	-0.0424	-0.0533	-0.0553	-0.1001	0.0541	0.0181	0.01	0.0445	0.0498	0.031
BTD only	0.0347	0.0293	-0.1151	-0.119	0.0193	0.0255	0.015	0.05	0.0358	0.0244

Table. S5 Bader charge analysis of BTD with different metal-doped Cu_2SnS_4 systems

* Bader charge values are reported in e^-;

System	O	C	H1	H2
$ZnCu_2SnS_4$ FA	-1.7192	1.6855	-0.0259	-0.02
FA only	-1.7679	1.6905	0.0706	0.0068
$MnCu_2SnS_4$ FA	-0.0543	-0.003	-0.0723	-0.0888
FA only	-0.0329	-0.0271	-0.0869	-0.0712
$TcCu_2SnS_4$ FA	-1.7698	1.6471	0.0401	-0.0067
FA only	-1.7475	1.7258	0.0106	0.0111
$ReCu_2SnS_4$ FA	-1.7634	1.6749	0.0077	0.0006
FA only	-1.737	1.6925	0.0068	0.0376

Table. S6 Bader charge analysis of FA with different metal-doped Cu_2SnS_4 systems

* Bader charge values are reported in e^-

System	VOC	Cl1	Cl2	Distance (Å)	Cl3	Adsorption energy (eV)	C1	ΔQ (e^-)	C2	ΔQ (e^-) of doped atoms	H
$ZnCu_2SnS_4$	-0.1140	-0.1588		-0.1842			0.2530	0.0469		0.1167	
$ZnCu_2SnS_4$ TCE	BTD			3.481		-0.232		-0.0317		Zn=+0.0024	
	FA			3.578		-0.139		-0.0796		Zn=+0.0052	
TCE only		-0.1523	-0.1551		-0.1770		0.2469	0.1415		0.0959	
$MnCu_2SnS_4$ TCE	TCE			3.521		-0.214		-0.0403		Zn=-0.032	
	BTD			3.268		-0.334		-0.0701		Mn=+0.0109	
$MnCu_2SnS_4$		-0.1896	-0.2063		-0.2018		0.2210	0.0987		0.1544	
TCE only		-0.1564	-0.1498		-0.1859		0.2539	0.1824		0.0559	
$TcCu_2SnS_4$ TCE		-0.2272	-0.2608		-0.2615		0.2570	0.1128		0.1195	
TCE only		-0.1622	-0.1476		-0.1903		0.2758	0.1260		0.0983	
$ReCu_2SnS_4$ TCE		-0.1891	-0.2053		-0.1755		0.2618	0.0926		0.1833	
TCE only		-0.1564	-0.1438		-0.1801		0.2688	0.1269		0.0845	

Table. S7 Bader charge analysis of TCE with different metal-doped Cu_2SnS_4 systems

* Bader charge values are reported in e^-

	FA	3.121	-0.49	-0.1811	Mn=+0.0541
	TCE	3.365	-0.385	-0.1237	Mn=-0.0148
$TcCu_2SnS_4$	**BTD**	3.491	-0.304	-0.0483	Tc=-0.0285
	FA	3.351	-0.165	-0.0893	Tc=+0.0303
	TCE	2.308	-1.152	-0.2602	Tc=+0.1512
$ReCu_2SnS_4$	**BTD**	3.518	-0.297	-0.0435	Re=-0.0105
	FA	3.278	-0.135	-0.0801	Re=+0.0457
	TCE	3.562	-0.372	-0.0321	Re=+0.0181

Table. S8 Bader charge analysis of BTD, FA and TCE at different metal-doped Cu_2SnS_4 systems

* ΔQ (VOC) values were obtained by subtracting the charges of only VOC from the charges of VOC in VOC-interacting metal-doped supercell systems ;

References

1 S. P. Selvam and S. Cho, *Surfaces and Interfaces*, 2025, **56**, 105610.

2 B. Chilukuri, U. Mazur and K. W. Hipps, *Appl. Sci.*, 2020, **10**, 740.

3 G. K. H. Madsen, J. Carrete and M. J. Verstraete, *Comput. Phys. Commun.*, 2018, **231**, 140–145.

4 A. Togo, *J. Phys. Soc. Japan*, 2023, **92**, 12001.

5 Y. Li, D. Bahamon, M. Sinnokrot and L. F. Vega, *npj Comput. Mater.*, 2022, **8**, 229.

6 A. Davariashtiyani and S. Kadkhodaei, *Commun. Mater.*, 2023, **4**, 105.

7 X. Yang, X. Qin, W. Yan, C. Zhang and D. Zhang, *Crystals*, , DOI:10.3390/cryst15090781.

8 A. Koufi, Y. Ziat and H. Belkhanchi, *Next Energy*, 2025, **9**, 100402.

9 L. Qiu, J. Xu and X. Tian, *Nanomaterials*, , DOI:10.3390/nano9111520.

10 V. Kochat, A. Apte, J. A. Hachtel, H. Kumazoe, A. Krishnamoorthy, S. Susarla, J. C. Idrobo, F. Shimojo, P. Vashishta, R. Kalia, A. Nakano, C. S. Tiwary and P. M. Ajayan, *Adv. Mater.*, 2017, **29**, 1703754.

11 T. Ratz, G. Brammertz, R. Caballero, M. León, S. Canulescu, J. Schou, L. Gütay, D. Pareek, T. Taskesen, D.-H. Kim, J.-K. Kang, C. Malerba, A. Redinger, E. Saucedo, B. Shin, H. Tampo, K. Timmo, N. D. Nguyen and B. Vermang, *J. Phys. Energy*, 2019, **1**, 42003.